Spin–Orbit Torque Switching in an All-Van der Waals Heterostructure

Inseob Shin, Won Joon Cho, Eun-Su An, Sungyu Park, Hyeon-Woo Jeong, Seong Jang, Woon Joong Baek, Seong Yong Park, Dong-Hwan Yang, Jun Ho Seo, Gi-Yeop Kim, Mazhar N. Ali, Si-Young Choi, Hyun-Woo Lee, Jun Sung Kim, Sung Dug Kim, and Gil-Ho Lee*

Current-induced control of magnetization in ferromagnets using spin–orbit torque (SOT) has drawn attention as a new mechanism for fast and energy efficient magnetic memory devices. Energy-efficient spintronic devices require a spin-current source with a large SOT efficiency (ξ) and electrical conductivity (σ), and an efficient spin injection across a transparent interface. Herein, single crystals of the van der Waals (vdW) topological semimetal WTe_2 and vdW ferromagnet Fe_3GeTe_2 are used to satisfy the requirements in their all-vdW-heterostructure with an atomically sharp interface. The results exhibit values of $\xi \approx 4.6$ and $\sigma \approx 2.25 \times 10^5 \ \Omega^{-1} \ m^{-1}$ for WTe_2. Moreover, the significantly reduced switching current density of 3.90×10^6 A cm^{-2} at 150 K is obtained, which is an order of magnitude smaller than those of conventional heavy-metal/ferromagnet thin films. These findings highlight that engineering vdW-type topological materials and magnets offers a promising route to energy-efficient magnetization control in SOT-based spintronics.

1. Introduction

Spintronics, a next-generation information technology, is based on effective spin-current generation and injection. Spin transfer torque (STT) induced by spin-polarized charge current injection across one ferromagnet (FM) layer into another has been successfully employed for the effective manipulation of magnetization, leading to the recent commercial STT-based magnetic memory solutions.[1] Spin–orbit torque (SOT), which uses out-of-plane spin current generated from in-plane charge current in high spin Hall effect (SHE) materials, can realize a more energy-efficient manipulation of magnetization and is reaching commercial maturity.[2–4] Thus far, various high spin–orbit coupling (SOC) materials, including heavy metals, topological insulators (TIs),[5–7] and recently, topological semimetals (TSMs),[8–11] have been studied to maximize their spin Hall angle, $\theta_{SH} = |J_s|/|J_c|$, a measure of their efficiency at converting charge current density J_c to spin current density J_s. Also, the interface engineering between the layers of high-SHE and FM materials has been investigated to maximize the spin transparency, T_{int}, across the interface.[12–19] The key challenge for efficient SOT spintronic devices is to maximize the SOT efficiency, $\xi = \theta_{SH} \cdot T_{int}$.[20]

Recent rapid developments in van der Waals (vdW) materials and their heterostructures provide new opportunities for

I. Shin, E.-S. An, H.-W. Jeong, S. Jang, J. H. Seo, H.-W. Lee, J. S. Kim, G.-H. Lee
Department of Physics
Pohang University of Science and Technology
Pohang 37673, Republic of Korea
E-mail: lghman@postech.ac.kr

W. J. Cho, W. J. Baek, S. Y. Park, S. D. Kim
Material Research Center
Samsung Advanced Institute of Technology (SAIT)
Samsung Electronics Co., Ltd., 130 Samsung-ro, Yeongtong-gu, Suwon-si, Gyeonggi-do 16678, Republic of Korea

The ORCID identification number(s) for the author(s) of this article can be found under https://doi.org/10.1002/adma.202101730.

E.-S. An, S. Park, J. S. Kim
Center for Artificial Low Dimensional Electronic Systems
Institute for Basic Science (IBS)
Pohang 37673, Republic of Korea

D.-H. Yang, G.-Y. Kim, S.-Y. Choi
Department of Materials Science and Engineering
Pohang University of Science and Technology
77 Cheongam-Ro, Pohang 37673, Republic of Korea

M. N. Ali
Max Planck Institute for Microstructure Physics
Weinberg 2, 06120 Halle (Saale), Germany

H.-W. Lee, G.-H. Lee
Asia Pacific Center for Theoretical Physics
77 Cheongam-Ro, Pohang 37673, Republic of Korea
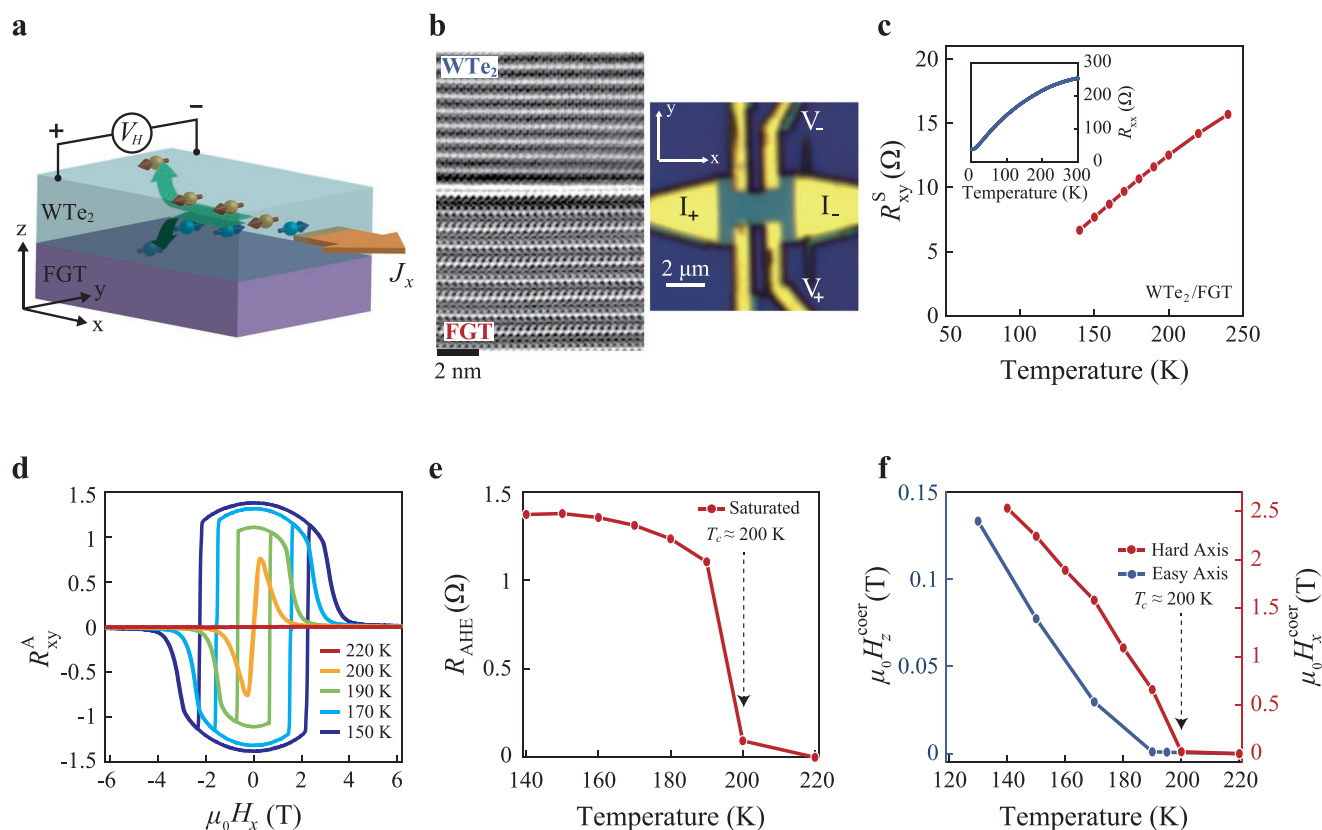
Figure 1. Structure of WTe_2/Fe_3GeTe_2 (FGT) device and electric and magnetic properties of FGT. a) Device schematics of a WTe_2/FGT heterostructure. The charge current (J_x, yellow arrow) applied to WTe_2 generates a spin current that is injected into the FGT along the $-z$-direction. By conservation of angular momentum, this spin current exerts a torque on the magnetization (M) of the FGT. Ball symbols with arrows represent electrons with their spin, respectively. b) Cross-sectional annular bright field scanning transmission electron microscopy image of WTe_2/FGT heterostructure viewed from [120] directions of FGT (left panel) and optical image of the Hall bar device (right panel). The current is applied along the x-axis, and the Hall voltage is measured along the y-axis. c) Temperature dependence of symmetric part of Hall resistance at zero field R_{xy}^S and longitudinal resistance R_{xx} (inset) of the WTe_2/FGT Hall bar device. d) Anti-symmetrized Hall resistance R_{xy}^A as a function of an in-plane magnetic field along the x-axis H_x at different temperatures. e,f) Temperature dependence of e) anomalous Hall resistance R_{AHE}, f) easy-axis (H_z^{coer}) and hard-axis (H_x^{coer}) coercive field of the device. The critical temperature T_c is ≈ 200 K.

improved spintronic functionalities. A large group of topological materials was identified in vdW structures with an atomically flat surface. Also recently, FM vdW materials have been discovered,[21,22] some of which exhibit a relatively high Curie temperature (T_C) and perpendicular magnetic anisotropy (PMA),[23] which is important for FM layers in spintronic devices. Thus far, topological and FM vdW materials have been used as one of the constituent layers, either for spin-current generation or as the FM layer, e.g., a vdW TI Bi_2Se_3 with a deposited FM CoFeB layer[7] or a vdW FM Fe_3GeTe_2 (FGT) with a deposited heavy-metal Pt layer.[24,25] While current-induced magnetization control was successfully demonstrated in both cases, SOT performance in all-vdW heterostructures has yet to be explored. Here, using a vdW heterostructures of the topological semimetal WTe_2 and ferromagnet Fe_3GeTe_2, we show efficient current-induced magnetization switching with a much smaller switching current and power dissipation, as compared to conventional SOT devices. These observations highlight that all-vdW heterostructure with vdW TSMs and ferromagnets provide a promising architecture for SOT-based spintronic devices.

2. Results and Discussion

Figure 1a schematically shows the spin Hall effect in WTe_2 producing a pure spin current, which is injected into the FGT layer, and exerts an SOT on the magnetization of FGT. In this study, we fabricated an all-vdW heterostructure consisting of WTe_2 (12.6 nm)/FGT (7.3 nm) using a dry transfer technique (Figure S1, Supporting Information). The exfoliation of WTe_2 and FGT crystals, and transfer processes were performed in an inert argon atmosphere glovebox. After capping the WTe_2/FGT stack with a 2.6 nm thick aluminium oxide layer without exposing it to air, we patterned the stack into a Hall bar shape; this was followed by electrode deposition, as shown in Figure 1b (device 1) (see Experimental Section and Figure S2, Supporting Information). The cross-sectional scanning transmission electron microscopic (STEM) image of a representative WTe_2/FGT stack clearly shows the atomic layers of WTe_2 and FGT with the atomically sharp interface between them. This confirms that vdW stacking produces a clean interface without any residue or intermixing (see Figures S3–S5 for detailed analysis on the interface, Supporting Information).

**ADVANCED
SCIENCE NEWS**

www.advancedsciencenews.com

**ADVANCED
MATERIALS**

www.advmat.de
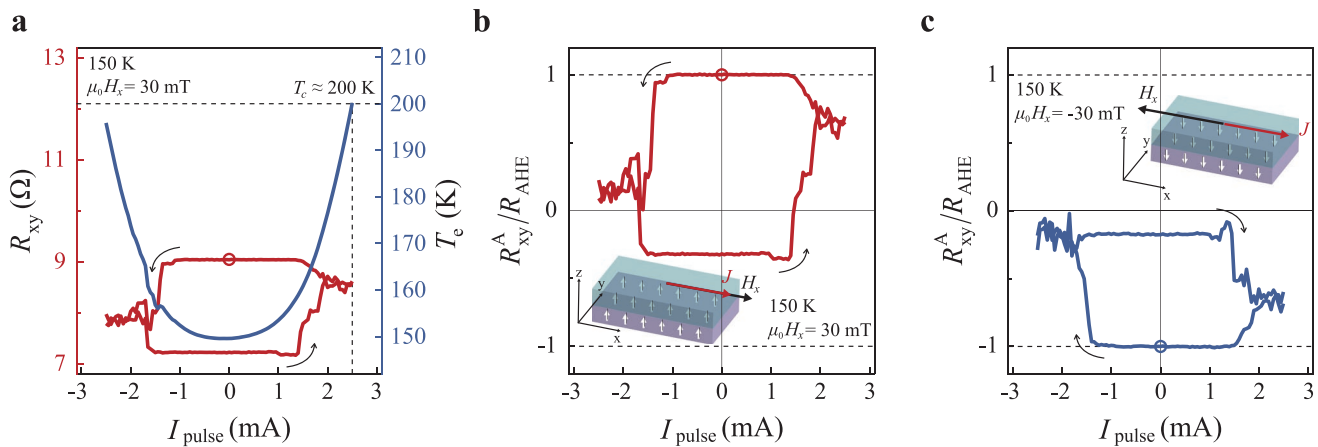
Figure 2. Current-induced magnetization switching in WTe$_2$/Fe$_3$GeTe$_2$ (FGT) heterostructure (device 1). a) Hall resistance R_{xy} (red line) measured after applying 10 ms long current pulses of height I_{pulse} in the presence of an in-plane magnetic field $\mu_0 H_x = 30$ mT parallel to the charge current at 150 K. μ_0 is a vacuum permeability. The initial state of FGT is saturated by the up-state ($M \parallel +z$-axis), which is denoted by a dot. Arrows indicate the I_{pulse}-sweep direction, and the switching polarity is anticlockwise. The electron temperature T_e (blue line) during the current pulse is plotted as a function of I_{pulse}. The dashed lines represent the critical temperature $T_c \sim 200$ K of FGT and the corresponding I_{pulse}. b,c) The ratio of R_{xy}^A to the anomalous Hall resistance R_{AHE} measured with a sweeping I_{pulse} under $\mu_0 H_x$ of b) 30 mT and c) −30 mT at 150 K. The switching polarity is anticlockwise for (b) and clockwise for (c). Dots denote the initial magnetization states of FGT. The horizontal dashed lines represent the states of saturated magnetization of FGT.

We first discuss the temperature and magnetic characteristics of the device. All the experimental data are measured in device 1, unless stated otherwise. Figure 1c shows the temperature dependence of the symmetrized Hall resistance (R_{xy}^S) and longitudinal resistance (R_{xx}) of the device, the former of which will be used later to estimate electronic temperature at a high bias current (see the temperature dependence of the WTe$_2$ layer in Figure S6, Supporting Information). Figure 1d–f presents the magnetic properties of the device. The anti-symmetrized Hall resistance $R_{xy}^A(H_x) = [R_{xy}(H_x) - R_{xy}(-H_x)]/2$ exhibits hysteretic behavior with the in-plane magnetic field H_x, owing to a slight misalignment of the magnetic field. This is a typical hard-axis hysteresis loop for the materials with PMA. As the temperature increases, the hysteresis gradually disappears, and the anomalous Hall resistance R_{AHE}, i.e., R_{xy}^A at $H_x = 0$, decreases and eventually vanishes at the critical temperature $T_c \sim 200$ K (Figure 1e), which is close to the bulk $T_c = 205-220$ K.[23,26] Hard- and easy-axis coercive fields (H_x^{coer} and H_z^{coer}, respectively) also vanish at a similar T_c, as shown in Figure 1f. The T_c of the device is comparable to those measured in FGT of similar thickness in previous studies,[23] thereby indicating no significant degradation of FGT during the device fabrication. Here, H_z^{coer} is measured in another FGT device (7.86 nm) of the same $T_c \sim 200$ K (Figure S7, Supporting Information).

We show that the SOT that originated from the charge current flowing through WTe$_2$ can deterministically switch the perpendicular FGT magnetization of the device in the presence of H_x. To measure current-induced magnetization switching, we first applied a 10 ms long write pulse of height I_{pulse}, and we subsequently measured R_{xy} with a read pulse of height of 10 μA. We kept 100 ms long delay between write and read pulses. As shown in **Figure 2**a, the switching of R_{xy} occurs at $I_{pulse} \sim \pm 1.5$ mA with an anticlockwise switching polarity for a positive H_x, which indicates a positive Hall angle in WTe$_2$.[27,28] Multiple sweeps of I_{pulse} show consistent and stable switching loops, which will be discussed later. Unlike conventional FMs

(e.g., Co or CoFeB), which have a T_c that is considerably higher than the operation temperature, FGT has a relatively low T_c, such that the Joule heating effect may significantly alter the device performance. Thus, we have further analyzed the elevation of the electronic temperature (T_e), owing to Joule heating from the current pulses (blue curve in Figure 2a). A slight misalignment between the Hall electrodes in the device introduces a small symmetric component in the Hall resistance. By comparing it with $R_{xy}^S(T)$ curve of Figure 1c, we were able to deduce the electronic temperature T_e during the current pulses (see Figure S8 for more details in deducing T_e for device 2, Supporting Information). While the rise of T_e ($\Delta T_e \sim 10$ K) is not significant at the switching I_{pulse} ($\approx \pm 1.5$ mA), T_e could approach T_c for the maximum I_{pulse} of 2.5 mA (see Figure S9, Supporting Information). For a stable measurement, we limited the maximum I_{pulse}, such that T_e did not exceed T_c. Figure 2b,c shows the switching of the normalized anti-symmetrized Hall resistance (R_{xy}^A/R_{AHE}) with opposite directions of H_x: $\mu_0 H_x = +30$ mT in Figure 2b and $\mu_0 H_x = -30$ mT in Figure 2c. As expected for the current-induced magnetization switching of PMA magnets by SOT, the switching polarity is opposite when reversing the direction of H_x.[2] Here, we used the value of R_{AHE} that we measured at 150 K in Figure 1e (see Figures S9–S11 for the discussion on Joule heating effect at high I_{pulse}). The observation that R_{xy}^A/R_{AHE} did not reach −1 for $\mu_0 H_x = +30$ mT or +1 for $\mu_0 H_x = -30$ mT can be explained by current spreading in the Hall bar device,[5] decrease of R_{AHE} with large bias current and in-plane magnetic field,[5] and/or multi-domain formation in FGT, owing to the Joule heating of T_e close to T_c, which will be discussed in further detail below.[24]

To further investigate the effect of Joule heating on the stability of the switching behavior, we measured the current-induced switching under three consecutive sweeps of current pulses with various maximum I_{pulse} (**Figure 3**a). When the maximum I_{pulse} is 2.5 mA, the maximum electronic temperature $T_{e,max} = 189$ K does not exceed $T_c = 200$ K for FGT, and
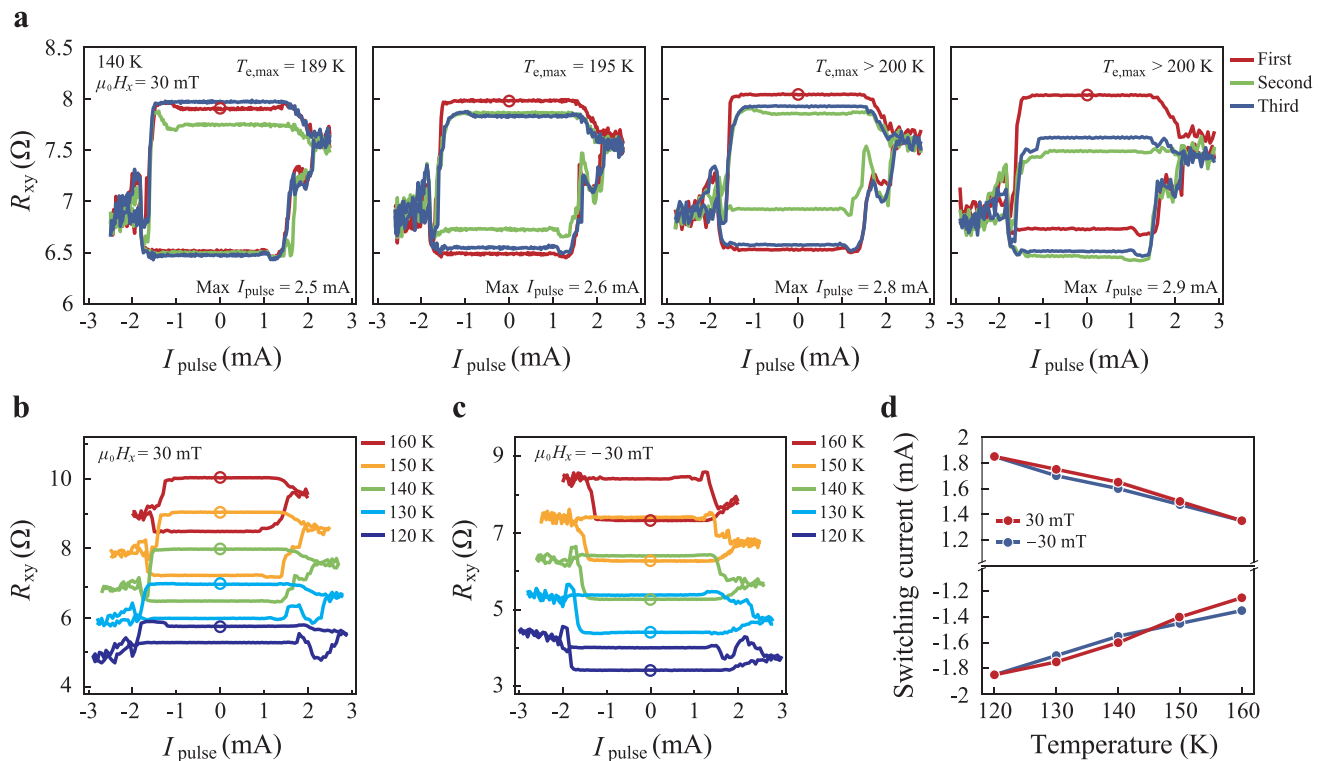
Figure 3. Current pulse height I_{pulse} and temperature dependence of current-induced magnetization switching. a) Hall resistance R_{xy} under three consecutive sweeps of I_{pulse} with in-plane magnetic field $\mu_0 H_x = 30$ mT at $T = 140$ K. The maximum value of I_{pulse} for each case is varied from 2.5 to 2.9 mA. The initial state of Fe_3GeTe_2 (FGT) is denoted by circles. For each case, the maximum electronic temperature $T_{e,max}$ was estimated as the electron temperature of the device during current pulses of maximum I_{pulse}. b,c) R_{xy} under sweeps of I_{pulse} at different temperatures with b) $\mu_0 H_x = 30$ mT and c) $\mu_0 H_x = -30$ mT. The initial state of FGT is denoted by dot symbols. d) Switching current as a function of temperature for $\mu_0 H_x = 30$ mT (red) and $\mu_0 H_x = -30$ mT (blue).

three consecutive sweeps show a relatively consistent current-induced switching. However, as the maximum I_{pulse} increases to 2.9 mA, $T_{e,max}$ becomes comparable to, or exceeds, T_c, and the current-induced switching behavior becomes more inconsistent for consecutive sweeps. For these cases, the magnetization of the device cannot return to its original state (see the case for device 2 in Figure S10, Supporting Information). We suspect that when $T_{e,max}$ exceeds T_c of FGT the significant thermal fluctuations induced by large bias current randomizes the magnetic domain of FGT and makes switching behavior unstable. This also emphasizes that the Joule heating issue is important to consider when using vdW FMs with a low T_c,[29] such as $Cr_2Ge_2Te_6$ or CrI_3.[21,22]

The temperature dependence of current-induced switching is shown in Figure 3b,c. The maximum I_{pulse} was limited so that $T_{e,max}$ did not exceed $T_c = 200$ K for FGT. The difference in the R_{xy} value at opposite magnetizations decreases with a decrease in T, which is attributed to changes in the current distribution between WTe_2 and FGT. At lower T, the resistivity of WTe_2 decreases significantly, while that of FGT remains almost constant; therefore, less current flowing through FGT results in a smaller Hall voltage. Figure 3d summarizes the temperature dependence of the switching current (Figures S12–16, Supporting Information). The reduction of the switching current with increasing T is due to the simultaneous decrease in the magnetization of FGT and the easy-axis coercive field.

Generally, the charge-to-spin conversion efficiency is quantified by the SOT efficiency $\xi = \frac{4e}{\pi\hbar} M_{FGT} t_{FGT} \frac{H_z^{coer}}{J_{sw}}$,[25,30–35] where e is the electron charge, $\hbar$ is the reduced Plank constant, M_{FGT} is the saturation magnetization of FGT, t_{FGT} is the thickness of FGT, H_z^{coer} is the easy-axis coercive field (Figure 1f), and J_{sw} is the switching current density of the device. From the parallel resistor model for WTe_2/FGT, we estimated that 60% of the total current flows through WTe_2 at $T_e \sim 160$ K ($T = 150$ K), which results in $J_{sw} = 3.90 \times 10^6$ A cm^{-2}. If taking $M_{FGT} = 240$ emu cm^{-3} and $H_z^{coer} = 522$ G at $T_e \sim 160$ K, we obtain $\xi = 4.6$. Here, M_{FGT} is measured in a bulk crystal of FGT with $T_c \sim 200$ K, which is similar to that of the SOT device discussed thus far (Figure S17, Supporting Information). Another device (device 2) consisting of 9.1 nm WTe_2 and 5.8 nm FGT reproduced current-induced magnetization switching with similar $\xi = 2.2$ (see Figures S18 and S19, Supporting Information).

We now discuss the SOT performance of our WTe_2/FGT device in comparison with previous SOT devices. First, we compare our WTe_2/FGT device to Pt/FGT devices that use the same FM material, FGT, but sputtered spin-current generation material, Pt. The switching current density J_{sw} of our WTe_2/FGT (3.90×10^6 A cm^{-2}) is an order of magnitude smaller than that of Pt/FGT devices. At a similar $T/T_c \sim 0.8$, the J_{sw} of Pt/FGT devices is 1.2×10^7 A cm^{-2} at 120 K[24] and 2.5×10^7 A cm^{-2} at 180 K.[25] Second, we compare our WTe_2/FGT device to

WTe$_2$/Py that uses the same spin-current generation material, WTe$_2$, but with sputtered FM, Py. WTe$_2$/Py device had a SOT efficiency $\xi = 0.09$–0.51 estimated with spin-torque ferromagnetic resonance measurement,[28] which is an order of magnitude smaller than our results ($\xi = 4.6$). These comparisons suggest that using WTe$_2$ as a spin-current generation material combined with FM layers through vdW stacking enhanced SOT performance, which can be attributed due to better spin transparency across the atomically sharp vdW interface. Here, we discuss two factors that can affect interfacial spin transparency: one is the roughness of the interface, and another is the electric potential gradient at the interface. Rough ferromagnetic interface has been suggested to create inhomogenous local magnetic field, which causes inhomogeneity of the spin precession and reduction of spin accumulation.[43] In this regards, atomically flat interface of all-vdW heterostructure is expected to be beneficial for better spin injection efficiency. On the contrary, several researches on transition metal ferromagnets and nonmagnetic materials argue that the rough interface or the intermixing of atoms near the interface may suppress the abrupt potential gradient and reduce the interface spin loss, leading to better spin transparency.[44,45]

In our WTe$_2$/FGT heterostructure, the terminated atoms in FGT, i.e., tellurium (Te), are the same as those in WTe$_2$, which can be strongly coupled through the 5p orbital.[46] According to the STEM and the energy dispersive X-ray spectroscopy analysis (see Figures S3–S5, Supporting Information), there is a Te-rich interfacial layer of single atomic thickness (≈ 0.3 nm), which was presumably formed by Te atoms escaped from FGT and/or WTe$_2$ crystals. The coupling between Te termination atoms of WTe$_2$ and Te termination layer of FGT via single atomic-layer thick Te-rich interfacial layer may have been beneficial for minimizing electron scattering and spin loss across WTe$_2$ and FGT layers. However, further experimental and theoretical investigation on the spin transparency of vdW interfaces is needed. Lastly, WTe$_2$ is a TSM with a large conductivity (2.25×10^5 Ω^{-1} m^{-1}), which is an order of magnitude larger than that of Bi$_x$Se$_{1-x}$ TIs (1.4–9.4×10^4 Ω^{-1} m^{-1})[5,7,41,47] or similar to that of narrow-gap TI Bi$_{0.9}$Sb$_{0.1}$ (2.5×10^5 Ω^{-1} m^{-1}).[6] In addition, the conductivity of FGT (2.69×10^5 Ω^{-1} m^{-1}) is ≈ 2–20 times smaller than that of conventional FMs, such as Co, Py, CoTb, and CoFeB (0.5–4.2×10^6 Ω^{-1} m^{-1}).[5,7,36,47] Therefore, a larger portion of current flows through the spin-current generation layer, and the dissipation power density of the whole device at magnetization switching (P_{sw}) is lowered as summarized in **Figure 4**, hence exhibiting improved energy efficiency.

3. Conclusions

Here, we outline a few directions to pursue to further enhance the functionalities of all-vdW heterostructures. Currently, various 2D ferromagnetic materials are actively being discovered and studied. Additional to Fe$_3$GeTe$_2$, which was used in this study, a series of Fe$_n$GeTe$_2$ ($3 \leq n \leq 5$) has been investigated theoretically and experimentally to enhance T_c and the saturation magnetization.[26] In addition to its vdW layered and single crystalline structure, the topological nodal-line structure of spin-polarized bands of FGT may also provide
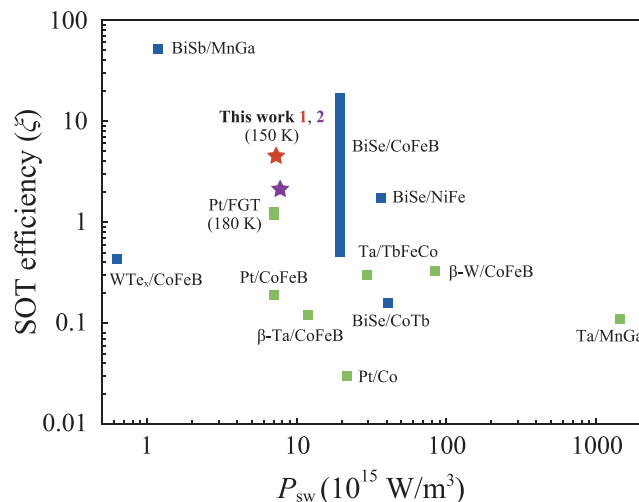
Figure 4. Comparison of spin–orbit torque (SOT) efficiency and dissipation power density for magnetization switching. Spin–orbit torque efficiency ξ estimated from the current-induced magnetization switching and dissipation power density of the whole device at magnetization switching (P_{sw}) for devices based on heavy metals (green symbols)[2,3,25,36–40] and topological materials (blue symbols)[5–7,41,42] at room temperature unless noted otherwise. Results from this work (devices 1 and 2) are denoted by star symbols. The vertical length of the bar represents the range of the parameter. "WTe$_x$" represents sputtered disordered WTe$_2$.

better performance for spintronic applications with a large spin Hall angle.[48] Also, a theoretical study[49] and a related experiment[50] suggest that owing to the lowered geometrical symmetries in the single FGT layer, the current flow in FGT layer may induce SOT, which can contribute to magnetization switching. Moreover, WTe$_2$ has exhibited out-of-plane anti-damping torque, which was induced by a current bias along the low-symmetry axis.[8,9,51] This is owing to its broken screw-axis and glide plane symmetries at the surfaces, which is not allowed for conventional HMs. Such unconventional SOT can enable current-induced magnetization switching without an external magnetic field, which is highly desirable for practical applications and also demonstrated recently.[52] Further optimization with novel topological materials, together with interface engineering, can lead to highly energy-efficient all-vdW spintronics devices.

4. Experimental Section

A WTe$_2$ (FGT) single crystal was mechanically exfoliated to provide WTe$_2$ (FGT) thin flakes with a thickness of 10–15 nm (< 10 nm) on Gel-Film PF-30/17-X4 from Delphon Industries (silicon oxide wafer). The WTe$_2$ flakes were transferred onto the FGT flake to make WTe$_2$/FGT vdW heterostructures. All the exfoliation and transfer processes were performed in an inert argon atmosphere glovebox to minimize the degradation of the materials and interfaces. To protect a stack of WTe$_2$/FGT during the fabrication process, aluminium oxide with a thickness of 2.6 nm was deposited via electron beam (e-beam) evaporation, without exposing the WTe$_2$/FGT stack to the air. The thickness of the WTe$_2$ and FGT flakes was confirmed using atomic force microscopy before the fabrication process. Electrodes were patterned using e-beam lithography, and in situ argon ion milling was used to eliminate the aluminium oxide of the WTe$_2$/FGT stack, followed by Cr (5 nm)/Au (35 nm) electrode

ADVANCED
SCIENCE NEWS

www.advancedsciencenews.com

ADVANCED
MATERIALS

www.advmat.de

deposition. Last, the WTe$_2$/FGT stack was shaped into Hall bar geometry using in situ argon ion milling, followed by aluminium oxide (50 nm) deposition to protect etched sides of the WTe$_2$/FGT stack from air exposure. Current direction of the WTe$_2$/FGT device was 23° off from *a*-axis of WTe$_2$ crystal.

Supporting Information

Supporting Information is available from the Wiley Online Library or from the author.

Conflict of Interest

The authors declare no conflict of interest.

Data Availability Statement

The data that support the findings of this study are available from the corresponding author upon reasonable request.

Keywords

[1] A. Brataas, A. D. Kent, H. Ohno, *Nat. Mater.* **2012**, *11*, 372.
[2] L. Liu, C.-F. Pai, Y. Li, H. W. Tseng, D. C. Ralph, R. A. Buhrman, *Science* **2012**, *336*, 555.
[3] I. M. Miron, K. Garello, G. Gaudin, P. J. Zermatten, M. V. Costache, S. Auffret, S. Bandiera, B. Rodmacq, A. Schuhl, P. Gambardella, *Nature* **2011**, *476*, 189.
[4] J. Ryu, S. Lee, K. J. Lee, B. G. Park, *Adv. Mater.* **2020**, *32*, 1907148.
[5] J. Han, A. Richardella, S. A. Siddiqui, J. Finley, N. Samarth, L. Liu, *Phys. Rev. Lett.* **2017**, *119*, 077702.
[6] N. H. D. Khang, Y. Ueda, P. N. Hai, *Nat. Mater.* **2018**, *17*, 808.
[7] M. Dc, R. Grassi, J. Y. Chen, M. Jamali, D. Reifsnyder Hickey, D. Zhang, Z. Zhao, H. Li, P. Quarterman, Y. Lv, M. Li, A. Manchon, K. A. Mkhoyan, T. Low, J. P. Wang, *Nat. Mater.* **2018**, *17*, 800.
[8] D. MacNeill, G. M. Stiehl, M. H. D. Guimarães, N. D. Reynolds, R. A. Buhrman, D. C. Ralph, *Phys. Rev. B* **2017**, *96*, 054450.
[9] D. MacNeill, G. M. Stiehl, M. H. D. Guimaraes, R. A. Buhrman, J. Park, D. C. Ralph, *Nat. Phys.* **2016**, *13*, 300.
[10] P. Li, W. Wu, Y. Wen, C. Zhang, J. Zhang, S. Zhang, Z. Yu, S. A. Yang, A. Manchon, X. X. Zhang, *Nat. Commun.* **2018**, *9*, 3990.
[11] B. Zhao, B. Karpiak, D. Khokhriakov, A. Johansson, A. M. Hoque, X. Xu, Y. Jiang, I. Mertig, S. P. Dash, *Adv. Mater.* **2020**, *32*, 2000818.
[12] X. Fan, H. Celik, J. Wu, C. Ni, K. J. Lee, V. O. Lorenz, J. Q. Xiao, *Nat. Commun.* **2014**, *5*, 3042.
[13] X. Qiu, K. Narayanapillai, Y. Wu, P. Deorani, D. H. Yang, W. S. Noh, J. H. Park, K. J. Lee, H. W. Lee, H. Yang, *Nat. Nanotechnol.* **2015**, *10*, 333.
[14] Y. W. Oh, S. H. Chris Baek, Y. M. Kim, H. Y. Lee, K. D. Lee, C. G. Yang, E. S. Park, K. S. Lee, K. W. Kim, G. Go, J. R. Jeong, B. C. Min, H. W. Lee, K. J. Lee, B. G. Park, *Nat. Nanotechnol.* **2016**, *11*, 878.
[15] J. C. Rojas-Sanchez, N. Reyren, P. Laczkowski, W. Savero, J. P. Attane, C. Deranlot, M. Jamet, J. M. George, L. Vila, H. Jaffres, *Phys. Rev. Lett.* **2014**, *112*, 106602.
[16] W. Zhang, W. Han, X. Jiang, S.-H. Yang, S. S. P. Parkin, *Nat. Phys.* **2015**, *11*, 496.
[17] W. Zhang, M. B. Jungfleisch, W. Jiang, Y. Liu, J. E. Pearson, S. G. E. t. Velthuis, A. Hoffmann, F. Freimuth, Y. Mokrousov, *Phys. Rev. B* **2015**, *91*, 115316.
[18] V. P. Amin, M. D. Stiles, *Phys. Rev. B* **2016**, *94*, 104420.
[19] S. C. Baek, V. P. Amin, Y. W. Oh, G. Go, S. J. Lee, G. H. Lee, K. J. Kim, M. D. Stiles, B. G. Park, K. J. Lee, *Nat. Mater.* **2018**, *17*, 509.
[20] F. Hellman, A. Hoffmann, Y. Tserkovnyak, G. S. D. Beach, E. E. Fullerton, C. Leighton, A. H. MacDonald, D. C. Ralph, D. A. Arena, H. A. Dürr, P. Fischer, J. Grollier, J. P. Heremans, T. Jungwirth, A. V. Kimel, B. Koopmans, I. N. Krivorotov, S. J. May, A. K. Petford-Long, J. M. Rondinelli, N. Samarth, I. K. Schuller, A. N. Slavin, M. D. Stiles, O. Tchernyshyov, A. Thiaville, B. L. Zink, *Rev. Mod. Phys.* **2017**, *89*, 025006.
[21] C. Gong, L. Li, Z. Li, H. Ji, A. Stern, Y. Xia, T. Cao, W. Bao, C. Wang, Y. Wang, Z. Q. Qiu, R. J. Cava, S. G. Louie, J. Xia, X. Zhang, *Nature* **2017**, *546*, 265.
[22] B. Huang, G. Clark, E. Navarro-Moratalla, D. R. Klein, R. Cheng, K. L. Seyler, D. Zhong, E. Schmidgall, M. A. McGuire, D. H. Cobden, W. Yao, D. Xiao, P. Jarillo-Herrero, X. Xu, *Nature* **2017**, *546*, 270.
[23] Y. Deng, Y. Yu, Y. Song, J. Zhang, N. Z. Wang, Z. Sun, Y. Yi, Y. Z. Wu, S. Wu, J. Zhu, J. Wang, X. H. Chen, Y. Zhang, *Nature* **2018**, *563*, 94.
[24] X. Wang, J. Tang, X. Xia, C. He, J. Zhang, Y. Liu, C. Wan, C. Fang, C. Guo, W. Yang, Y. Guang, X. Zhang, H. Xu, J. Wei, M. Liao, X. Lu, J. Feng, X. Li, Y. Peng, H. Wei, R. Yang, D. Shi, X. Zhang, Z. Han, Z. Zhang, G. Zhang, G. Yu, X. Han, *Sci. Adv.* **2019**, *5*, eaaw8904.
[25] M. Alghamdi, M. Lohmann, J. Li, P. R. Jothi, Q. Shao, M. Aldosary, T. Su, B. P. T. Fokwa, J. Shi, *Nano Lett.* **2019**, *19*, 4400.
[26] J. Seo, D. Y. Kim, E. S. An, K. Kim, G.-Y. Kim, S.-Y. Hwang, D. W. Kim, B. G. Jang, H. Kim, G. Eom, S. Y. Seo, R. Stania, M. Muntwiler, J. Lee, K. Watanabe, T. Taniguchi, Y. J. Jo, J. Lee, B. I. Min, M. H. Jo, H. W. Yeom, S.-Y. Choi, J. H. Shim, J. S. Kim, *Sci. Adv.* **2020**, *6*, eaay8912.

[27] B. Zhao, D. Khokhriakov, Y. Zhang, H. Fu, B. Karpiak, A. M. Hoque, X. Xu, Y. Jiang, B. Yan, S. P. Dash, *Phys. Rev. Res.* **2020**, *2*, 013286.

[28] S. Shi, S. Liang, Z. Zhu, K. Cai, S. D. Pollard, Y. Wang, J. Wang, Q. Wang, P. He, J. Yu, G. Eda, G. Liang, H. Yang, *Nat. Nanotechnol.* **2019**, *14*, 945.

[29] Y. Shao, W. Lv, J. Guo, B. Qi, W. Lv, S. Li, G. Guo, Z. Zeng, *Appl. Phys. Lett.* **2020**, *116*, 092401.

[30] T.-Y. Chen, C.-T. Wu, H.-W. Yen, C.-F. Pai, *Phys. Rev. B* **2017**, *96*, 104434.

[31] P. P. Haazen, E. Mure, J. H. Franken, R. Lavrijsen, H. J. Swagten, B. Koopmans, *Nat. Mater.* **2013**, *12*, 299.

[32] M. Hayashi, J. Kim, M. Yamanouchi, H. Ohno, *Phys. Rev. B* **2014**, *89*, 144425.

[33] J. Kim, J. Sinha, M. Hayashi, M. Yamanouchi, S. Fukami, T. Suzuki, S. Mitani, H. Ohno, *Nat. Mater.* **2013**, *12*, 240.

[34] A. Thiaville, S. Rohart, É. Jué, V. Cros, A. Fert, *Europhys. Lett.* **2012**, *100*, 57002.

[35] L. Zhu, D. C. Ralph, R. A. Buhrman, eprints, arXiv:2101.10521, **2021**.

[36] L. Liu, O. J. Lee, T. J. Gudmundsen, D. C. Ralph, R. A. Buhrman, *Phys. Rev. Lett.* **2012**, *109*, 096602.

[37] K. Meng, J. Miao, X. Xu, Y. Wu, J. Xiao, J. Zhao, Y. Jiang, *Sci. Rep.* **2016**, *6*, 38375.

[38] H.-Y. Lee, S. Kim, J.-Y. Park, Y.-W. Oh, S.-Y. Park, W. Ham, Y. Kotani, T. Nakamura, M. Suzuki, T. Ono, K.-J. Lee, B.-G. Park, *APL Mater.* **2019**, *7*, 031110.

[39] C.-F. Pai, L. Liu, Y. Li, H. W. Tseng, D. C. Ralph, R. A. Buhrman, *Appl. Phys. Lett.* **2012**, *101*, 122404.

[40] Z. Zhao, M. Jamali, A. K. Smith, J.-P. Wang, *Appl. Phys. Lett.* **2015**, *106*, 132404.

[41] Y. Wang, D. Zhu, Y. Wu, Y. Yang, J. Yu, R. Ramaswamy, R. Mishra, S. Shi, M. Elyasi, K. L. Teo, Y. Wu, H. Yang, *Nat. Commun.* **2017**, *8*, 1364.

[42] X. Li, P. Li, V. D.-H. Hou, M. D. C. , C.-H. Nien, F. Xue, D. Yi, C. Bi, C.-M. Lee, S.-J. Lin, W. Tsai, Y. Suzuki, S. X. Wang, eprint, arXiv: 2001.04054, **2020**.

[43] S. P. Dash, S. Sharma, J. C. Le Breton, J. Peiro, H. Jaffrès, J. M. George, A. Lemaître, R. Jansen, *Phys. Rev. B* **2011**, *84*, 054410.

[44] X. Tao, Q. Liu, B. Miao, R. Yu, Z. Feng, L. Sun, B. You, J. Du, K. Chen, S. Zhang, L. Zhang, Z. Yuan, D. Wu, H. Ding, *Sci. Adv.* **2018**, *4*, eaat1670.

[45] L. Zhu, D. C. Ralph, R. A. Buhrman, *Phys. Rev. B* **2019**, *99*, 180404(R).

[46] Y. Wu, S. Zhang, J. Zhang, W. Wang, Y. L. Zhu, J. Hu, G. Yin, K. Wong, C. Fang, C. Wan, X. Han, Q. Shao, T. Taniguchi, K. Watanabe, J. Zang, Z. Mao, X. Zhang, K. L. Wang, *Nat. Commun.* **2020**, *11*, 3860.

[47] A. R. Mellnik, J. S. Lee, A. Richardella, J. L. Grab, P. J. Mintun, M. H. Fischer, A. Vaezi, A. Manchon, E. A. Kim, N. Samarth, D. C. Ralph, *Nature* **2014**, *511*, 449.

[48] K. Kim, J. Seo, E. Lee, K. T. Ko, B. S. Kim, B. G. Jang, J. M. Ok, J. Lee, Y. J. Jo, W. Kang, J. H. Shim, C. Kim, H. W. Yeom, B. Il Min, B. J. Yang, J. S. Kim, *Nat. Mater.* **2018**, *17*, 794.

[49] O. Johansen, V. Risinggard, A. Sudbo, J. Linder, A. Brataas, *Phys. Rev. Lett.* **2019**, *122*, 217203.

[50] K. Zhang, S. Han, Y. Lee, M. J. Coak, J. Kim, I. Hwang, S. Son, J. Shin, M. Lim, D. Jo, K. Kim, D. Kim, H. W. Lee, J. G. Park, *Adv. Mater.* **2020**, *33*, 2004110.

[51] B. Zhao, A. M. Hoque, D. Khokhriakov, B. Karpiak, S. P. Dash, *Appl. Phys. Lett.* **2020**, *117*, 242401.

[52] I.-H. Kao, R. Muzzio, H. Zhang, M. Zhu, J. Gobbo, D. Weber, R. Rao, J. Li, J. H. Edgar, J. E. Goldberger, J. Yan, D. G. Mandrus, J. Hwang, R. Cheng, J. Katoch, A. S. Singh, eprint, arXiv: 2012.12388, **2020**.

2101730 (7 of 7)